



1 **A model for interpreting the deformation mechanism of reservoir landslides in the**
2 **Three Gorges Reservoir area, China**

3 Zongxing Zou¹, Huiming Tang¹, Robert E. Criss², Xinli Hu³, Chengren Xiong¹, Qiong
4 Wu³, Yi Yuan⁴

5 ¹Three Gorges Research Center for geo-hazards, China University of Geosciences, Wuhan, 430074,
6 China

7 ²Department of Earth and Planetary Sciences, Washington University, One Brookings Drive, Saint
8 Louis, United States

9 ³Faculty of Engineering, China University of Geosciences, Wuhan, 430074, China

10 ⁴Department of Land and Resources of Hubei Province, Wuhan, 430074, China

11 *Correspondence author: Huiming Tang (tanghm@cug.edu.cn)*

12



13 **Abstract.** Landslides whose slide surface is gentle near the toe and relatively steep in the middle
14 and rear part are common in the Three Gorges Reservoir area, China. The mass that overlies the
15 steep part of the slide surface is termed the “driving section” and that which overlies the gentle part
16 of the slide surface is termed the “locking section”. A driving-locking model is presented to elucidate
17 the deformation mechanism of reservoir landslides of this type, as exemplified by Shuping landslide.
18 More than 13 years of field observations that include rainfall, reservoir level and deformation show
19 that the deformation velocity of Shuping landslide depends strongly on the reservoir level but only
20 slightly on rainfall. Seepage modelling shows that the landslide was destabilized shortly after the
21 reservoir was first impounded to 135 m, which initiated a period of steady deformation from 2003 to
22 2006 that was driven by buoyancy forces on the locking section. Cyclical water-level fluctuations in
23 subsequent years also affected slope stability, with annual “jumps” in displacement coinciding with
24 drawdown periods that produce outward seepage forces. In contrast, the inward seepage force that
25 results from rising reservoir levels stabilizes the slope, as indicated by decreased deformation
26 velocity. Corrective transfer of earth mass from the driving section to the locking section
27 successfully reduced the deformation of Shuping landslide, and is a feasible treatment for huge
28 reservoir landslides in similar geological settings.

29 **Keywords:** Three Gorges Reservoir, Reservoir landslide, Water level fluctuation, Deformation
30 mechanism, Shuping landslide

31



32 **1 Introduction**

33 Reservoir landslides attract wide attention as they can cause huge surge waves and other
34 disastrous consequences (Huang et al., 2017; Wen et al., 2017; Froude and Petley, 2018). The surge
35 wave produced by the 1963 Vajont landslide in Italy destroyed Longarone village and caused nearly
36 2,000 fatalities (Paronuzzi and Bolla, 2012). A similar surge associated with the 2003 Qianjiangping
37 landslide, which slipped shortly after the Three Gorges Reservoir (TGR) in China was first
38 impounded, capsized 22 fishing boats and took 24 lives (Xiao et al., 2007; Tang et al., 2019). To
39 ensure the safety of the reservoir, 1.5 billion US dollars have been invested to reinforce the reservoir
40 banks in TGR. However, reinforcement structures are costly and difficult to construct, and thus many
41 huge reservoir landslides have not been treated (Wang and Xu, 2013). Many remain in a state of
42 continuous deformation, such that cumulative monitored displacements of several meters are now
43 documented at the Huangtupo (Tang et al., 2015; Dumperth et al., 2016), Outang (Yin et al., 2016),
44 and Baishuihe (Li et al., 2010; Du et al., 2013) landslides. Additional study of the deformation and
45 failure mechanisms, and risk reduction strategies of these huge reservoir landslides is of great
46 significance.

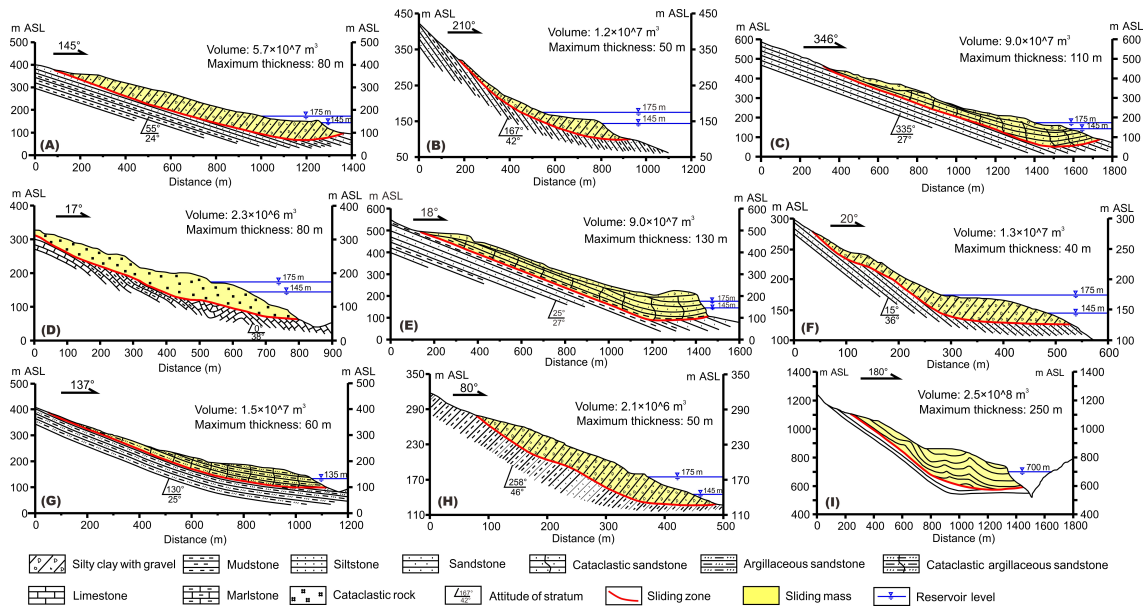
47 Most research on the deformation or failure mechanism of reservoir landslides involves
48 numerical modelling, physical model testing, or field observation. Many numerical simulations have
49 studied how landslide geometry, material permeability, variation rate of water level and pressure
50 variation influence the stability of reservoir landslides (Rinaldi and Casagli, 1999; Lane and Griffiths,
51 2000; Liao et al., 2005; Cojean and Cai, 2011; Song et al., 2015). Both small-scale (Junfeng et al.,



52 2004; Hu et al., 2005; Miao et al., 2018) and large-scale physical model experiments (Jia et al., 2009)
53 have been conducted to investigate the deformation features of reservoir landslides related to water
54 level change. Casagli et al. (1999) and Rinaldi et al. (2004) monitored the pore water pressure in
55 riverbanks to determine its effect on bank stability.

56 Since the impoundment of TGR, monitoring systems have been installed on or within many
57 reservoir landslides (Ren et al., 2015; Huang et al., 2017; Song et al., 2018; Wu et al., 2019), which
58 provide valuable data for the study of their deformation features. Several studies show that reservoir
59 water level variations and rainfall are the most critical factors that govern the deformation velocities
60 of reservoir landslides in TGR (Li et al., 2010; Tang et al., 2015; Ma et al., 2016; Wang et al., 2014).
61 Unfortunately, the effects of rainfall and reservoir level are difficult to distinguish because the period
62 of TGR drawdown is managed to coincide with the rainy season. Detailed deformation studies that
63 incorporate long-term continuous monitoring data are needed to quantify how periodic water-level
64 variations affect reservoir landslides. Moreover, the evolutionary trend of these deforming landslides
65 and feasible treatments for these huge reservoir landslides are rarely studied.

66 This study presents a model combined with seepage simulations to elucidate how reservoir
67 landslides deform, using the Shuping landslide as an example. The new environmental and
68 deformation data provided here extend the observational period for this landslide to more than 13
69 years, and include results that confirm the effectiveness of a control strategy that have been
70 implemented.



71

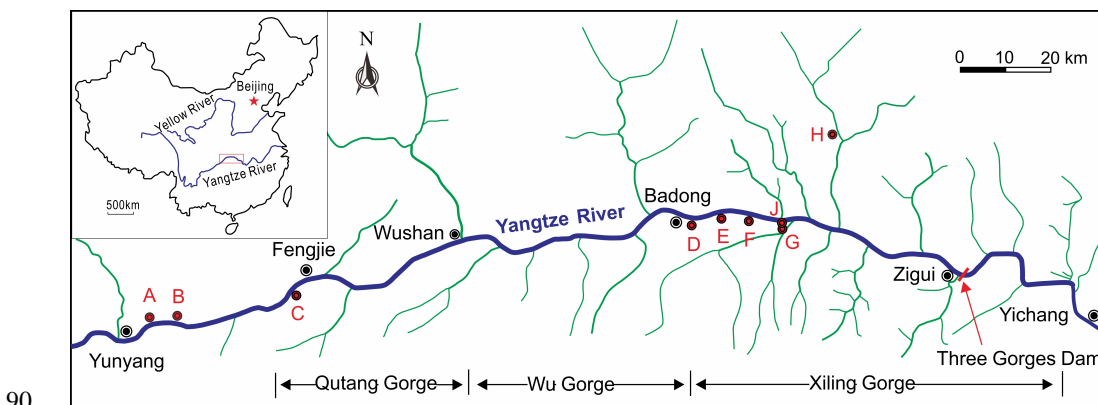
72 **Fig. 1** Geological profiles for typical reservoir landslides, all in the TGR except Vajont in Italy (I).
 73 (A) Jiuxianping landslide (Wang, 2013); (B) Xicheng landslide (Song, 2011); (C) Outang landslide
 74 (Yin et al., 2016); (D) No.1 riverside slump of Huangtupo landslide (Wang et al., 2014); (E)
 75 Muyubao landslide (Lu, 2012); (F) Baishuihe landslide (Lu, 2012); (G) Qiangjiangping landslide
 76 (Xiao et al., 2007); (H) Ganjuyuan landslide (Qin, 2011); (I) Vajont landslide, the world famous
 77 reservoir-induced landslide in Italy (Paronuzzi and Bolla, 2012). See Fig. 2 for locations.



78 2 A geomechanical model for reservoir-induced landslide

79 2.1 Typical reservoir-induced landslides in the Three Gorges Reservoir

80 Figure 1 and Fig. 2 summarize the reservoir landslides of most concern in the TGR plus the
81 world famous Vajont landslide. These landslides have many common features. First, all these
82 landslides have large volumes, ranging from millions of cubic meters to tens of millions of cubic
83 meters, and all are difficult to reinforce by conventional structures such anti-slide pile, retaining wall
84 etc. Second, the front part of the slide mass is always thicker than the rear part, with a maximum
85 thickness from 40 m to over 100 m. Another important feature of these profiles (Fig. 1) is that the
86 slope of the slide surface decreases gradually from the rear to the front and may become horizontal
87 or even anti-dip in the front. Last, these landslides were reactivated after the reservoir impoundment,
88 with large observed deformations indicating their metastable situation. All these features are relevant
89 to the deformation behavior of reservoir landslides, as discussed below.

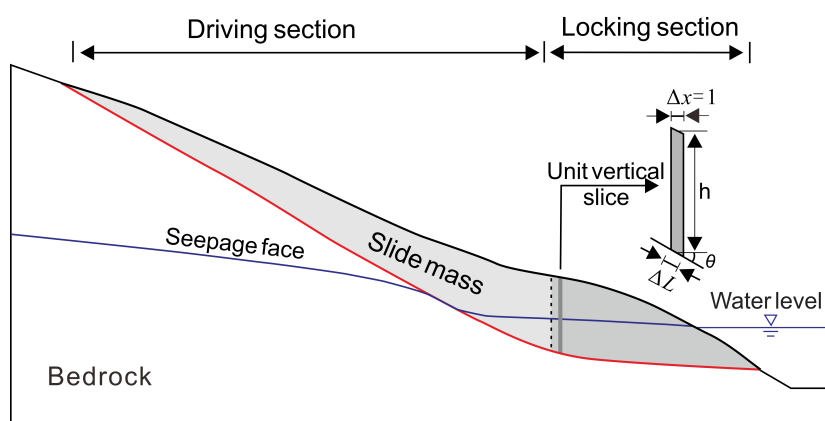


90
91 **Fig. 2** Location map for important landslides in TGR. Jiuxianping landslide (A); Xicheng landslide
92 (B); Outang landslide (C); Huangtupo landslide (D); Muyubao landslide (E); Baishuihe landslide (F);
93 Qiangjiangping landslide (G); Ganjuyuan landslide (H); Shuping landslide (J), Case study.



94 **2.2 Driving-locking model**

95 Due to the relatively high slope of the slide surface in the middle and rear part, the slide force
96 exceeds the resistance force on the proximal slide surface, producing extra thrust on the lower-front
97 slide mass. Consequently, the rear-upper is termed the “driving section” (Fig. 3). In contrast, the
98 potential slide surface underlying the lower-front part of the slide mass provides more resistance due
99 to the relatively gentle slide surface slope and greater thickness of the slide mass. The lower-front
100 part of the slide mass is termed the “locking section” (Fig. 3), as it blocks the driving section, thereby
101 playing a critical role in landslide stability (Tang et al., 2015).



102

103

Fig. 3 Driving-locking model for reservoir landslide

104 The locking section is defined as the lower-front part of the slide mass, where each unit vertical
105 slice (Fig. 3) can be self-stabilized under its self-weight. According to the limit equilibrium method
106 and the definition of the locking section, the sliding force of each vertical slice is the component of
107 its gravitational force along the slide surface, which cannot exceed the shear resistance provided by
108 the base. The special position where the sliding force of the vertical slice equals the resistance force



109 provided by the slide surface is regarded as the boundary between the driving and locking sections.

110 Force balance along the sliding direction for this special vertical slice can be written as

$$111 \quad w \sin \theta_1 = w \cos \theta_1 \tan \varphi + c \Delta L \quad (1)$$

112 where w is the weight of the unit vertical slice; θ_1 is the slope angle of the slide surface at the
113 boundary between the driving and locking sections; ΔL is the length of the slice base (see Fig. 3);
114 and c and φ are the cohesion and internal friction angle of the slide surface, respectively.

115 The weight of the slice $w = \gamma h \Delta x$, where γ is the unit weight of the slide mass, h is the vertical
116 distance from the center of the base of the slice to the ground surface, Δx is the unit width of the slice,
117 and $\Delta L = \Delta x / \cos \theta_1$ (Fig. 3). Thus Eq. (1) can be rewritten as

$$118 \quad \tan \theta_1 = f + k / \cos^2 \theta_1 \quad (2)$$

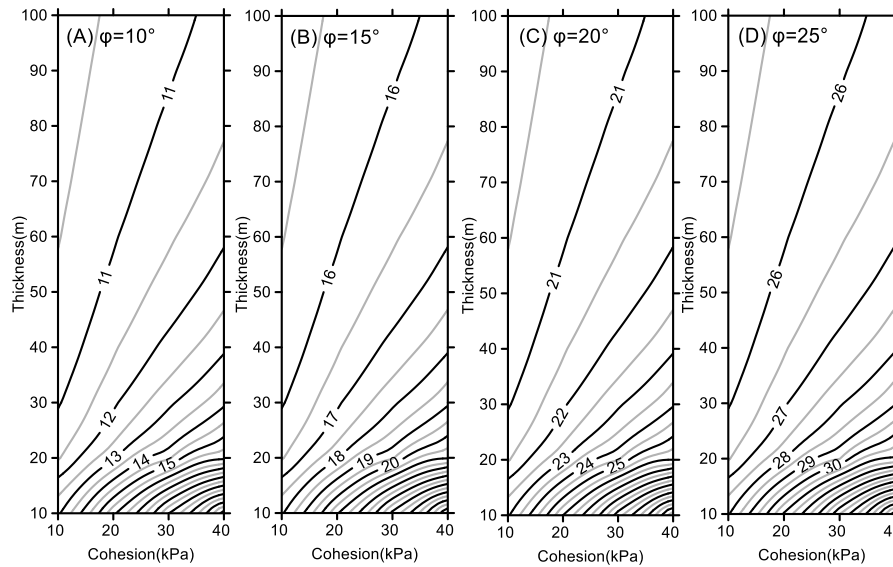
119 where $f = \tan \varphi$, $k = c / \gamma h$.

120 The solution to Eq. (2) provides the slope angle θ_1 of the slide surface:

$$121 \quad \theta_1 = 0.5 \arcsin T \quad (3)$$

$$122 \quad \text{where } T = \frac{(2k + f) + \sqrt{(2k + f)^2 - 4k(k + f)(1 + f^2)}}{1 + f^2}$$

123 Empirical values for the cohesion of the slide surface is less than 40 kPa, while the internal
124 friction angle of the slide surface varies between 10° and 25° (Chang et al., 2007), and the unit
125 weight of the soil is typically about 20 kN/m^3 . In order to further elucidate the effect of various
126 parameters on the length of the locking section, contour maps of θ_1 under different shear strength
127 parameters c and φ and the thickness of the slide mass h are plotted (Fig. 4), as derived from Eq. (3).



128

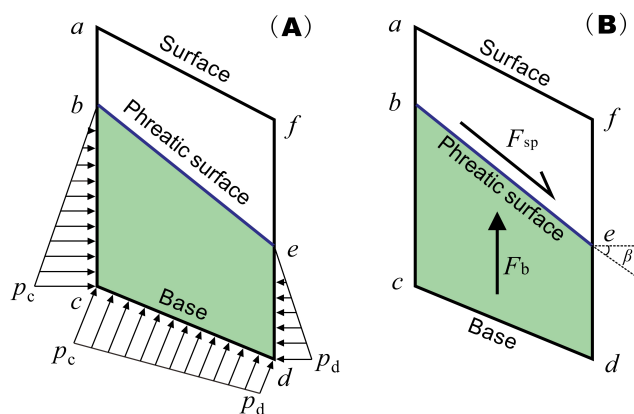
129 **Fig. 4** Contour maps for the slope angle θ_1 of slide surface that denotes the boundary between the
130 driving and locking sections under various shear strength parameters and slide mass thickness.

131 Figure 4 shows that θ_1 increases as the internal friction angle φ increases; however, by
132 comparison of the pattern and the values of the contour in the four sub-figures, the difference
133 between θ_1 and φ has little relationship to φ . Due to the effect of cohesion, θ_1 is always larger than φ
134 as shown in Fig. 4. As the cohesion c decreases, the difference between θ_1 and φ decreases, and for
135 cohesionless material with $c=0$, θ_1 is equal to φ . Fig. 4 also shows that when the thickness of the slide
136 mass reaches about 40 m, the difference between θ_1 and φ is very small (less than 3°), which
137 becomes even less as the thickness increases. These results indicate that for the thick slide mass (up
138 to 40 m), the boundary between the locking and driving sections can be approximated as the position
139 where the slope angle θ_1 equals the internal friction angle φ .



140 **2.3 Effect of water force on the locking and driving sections**

141 The impacts of the water level change on the reservoir slope stability can be quantified by
 142 analyzing the changes in water force on the slope. Lambe and Whitman (2008) have demonstrated
 143 that the water forces acting on an element of the slope can be equivalently expressed by either the
 144 ambient pore-water pressure (Fig. 5A) or by seepage and buoyancy forces (Fig. 5B). The latter form,
 145 i.e., seepage and buoyancy forces, are employed here to clarify the mechanical mechanism of water
 146 force on the reservoir bank.



147
 148 **Fig. 5** Two equivalent ways to display the water force acting on a slice of the slide mass. (A)
 149 expressed by pore-water pressure; (B) expressed by the seepage force F_{sp} and the buoyancy force F_b .

150 The seepage force (F_{sp}) represents the frictional drag of water flowing through voids that is
 151 proportional to the hydraulic gradient and acts in the direction of flow. It can be expressed as (Lambe
 152 and Whitman, 2008)

153
$$F_{sp} = \gamma_w i V \tag{4}$$

154 Where γ_w is the unit weight of water; i is the hydraulic gradient and equals $\sin\beta$ where β is the slope
 155 angle of the phreatic surface; V is the submerged volume of the analyzed element as the trapezoid



156 area enclosed by points *bcd*e in Fig. 5.

157 When the groundwater flows outwards as occurs during reservoir level drops, the corresponding
 158 outward seepage force decreases the slope stability. In contrast, the seepage force will be directed
 159 inward during reservoir level rise, increasing slope stability.

160 The buoyancy force (F_b) of the water exerted on the element can be expressed as

$$161 \quad F_b = \gamma_w V \quad (5)$$

162 The factor of safety (Fos) used to quantify the slope stability can be defined as the ratio of the
 163 shear strength (resistance, F_r) along the potential failure surface to the sliding force (F_s) by the
 164 Mohr-Coulomb failure criterion (Wang et al., 2014):

$$165 \quad Fos = \frac{F_r}{F_s} = \frac{\sum_{j=1}^n [c\Delta L_j + N_j \tan \varphi]}{\sum_{j=1}^n w_j \sin \theta_j} \quad (6)$$

166 where n is the total number of slices; N is the normal force on the base of each slice, and the other
 167 symbols are as above. Suppose that the variation of the effective slide mass weight in a slice is Δw ,
 168 due to the change of buoyancy force, which thereby modifies the resistance and sliding forces by ΔF_r
 169 and ΔF_s respectively. The corresponding change of the factor of safety ΔFos is:

$$170 \quad \Delta Fos = \frac{F_r + \Delta F_r}{F_s + \Delta F_s} - \frac{F_r}{F_s} = \frac{\Delta F_r * F_s}{(F_s + \Delta F_s) F_s} \left(1 - \frac{Fos}{\Delta F_r / \Delta F_s} \right) \quad (7)$$

171 The ratio of ΔF_r to ΔF_s for a vertical slice due to the change of its effective weight Δw is
 172 approximately:

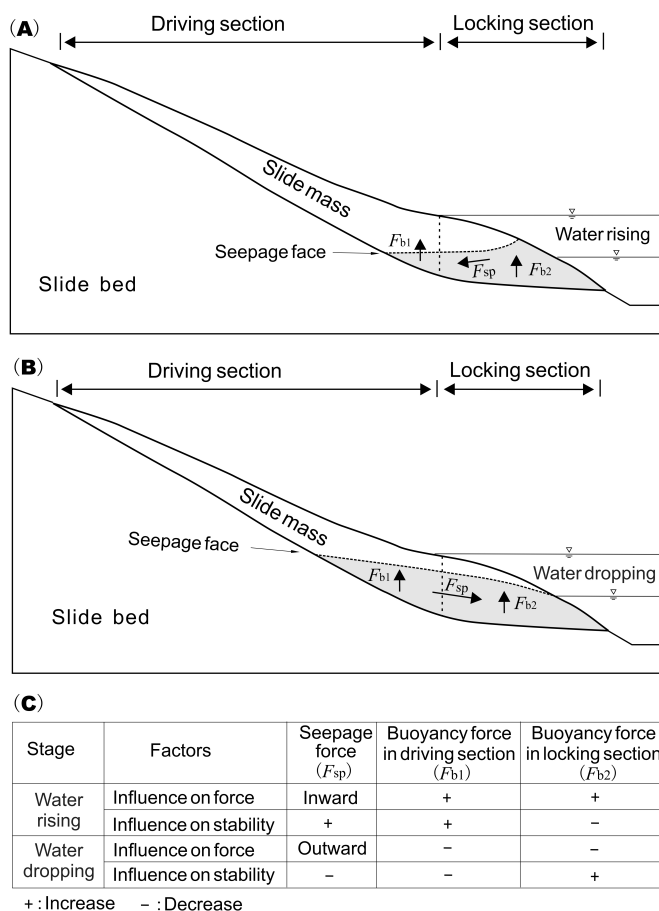
$$173 \quad \frac{\Delta F_r}{\Delta F_s} = \frac{\Delta w \cos \theta \tan \varphi}{\Delta w \sin \theta} = \frac{\tan \varphi}{\tan \theta} \quad (8)$$

174 Suppose that $\theta_2 = \arctan\left(\frac{\tan \varphi}{Fos}\right)$, where the change of the vertical slice weight has no influence



175 on the current stability ($\Delta F_{os}=0$). If $\theta<\theta_2$ and $\Delta w>0$, then $\Delta F_{os}>0$, indicating that increase of the
176 weight of lower-front part of the slide mass where its slope angle of the slide surface θ is less than θ_2
177 will improve the stability of the whole slide mass; conversely, decrease of the weight of the
178 lower-front part would decrease stability. In contrast, the upper-rear part has a contrary tendency. As
179 mentioned above, continuously deformed reservoir landslides are metastable and their corresponding
180 F_{os} is around 1; hence $\theta_2\approx\phi$. Consequently, in the cases that reservoir landslide is under metastable
181 state and has a thickness up to 40 m, $\theta_1\approx\theta_2\approx\phi$, the locking section and driving section have the same
182 mechanical behavior as described above. Either an increase in the weight of the locking section or a
183 decrease in the weight of the driving section will improve the stability of the slope and vice versa.

184 In summary, the effect of ground water on the slope or landslide stability can be resolved into a
185 seepage force and a buoyancy force. The effect of the seepage force on slope stability depends on the
186 direction and magnitude of flow. Buoyant forces change the effective weight of the slide mass and
187 have contrary effect on the locking and driving sections. On the basis of these rules, the mechanical
188 mechanism for reservoir-induced landslide can be illustrated as Fig. 6.



189

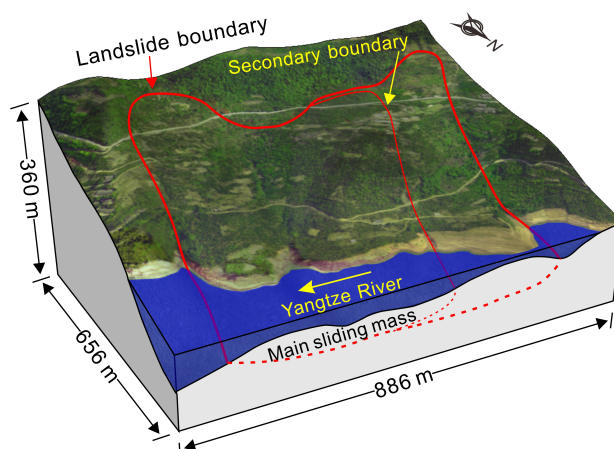
190 **Fig. 6** Mechanical mechanism for reservoir-induced landslide. (A) water level rise; (B) water level
 191 drop; (C) effects of various mechanisms on the landslide stability during water level rise and drop.

192 3 Shuping landslide

193 Shuping landslide is located in Shazhenxi Town, Zigui County, Hubei Province, on the south
 194 bank of the Yangtze River, 47 km upstream from the Three Gorges dam (Fig. 2). After the first
 195 impoundment of the reservoir in 2003, serious deformation was observed that endangered 580
 196 inhabitants and navigation on the Yangtze River (Wang et al., 2007). Previous studies of the Shuping
 197 landslide utilized GPS extensometers (Wang et al., 2007), or field surveys (Lu et al., 2014) to clarify



198 the deformation. This study provides a detailed geomechanical model that includes seepage and
199 buoyancy effects to clarify the deformation mechanism of this landslide which is calibrated by
200 long-term monitoring data.



201

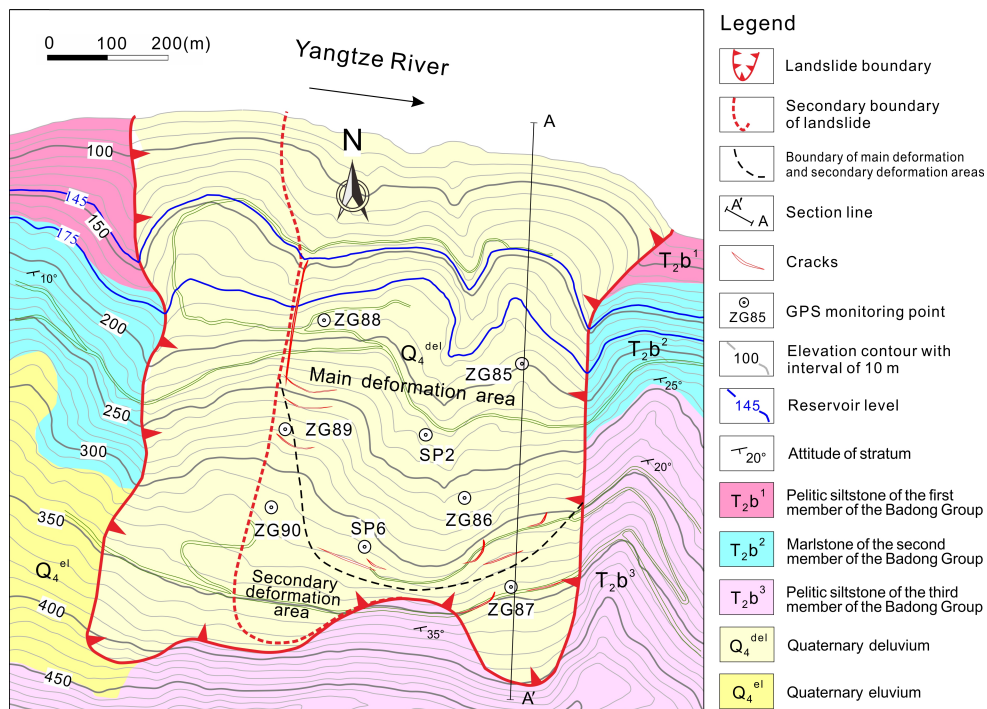
202 **Fig. 7** Full view of Shuping landslide (the surface satellite map © Google Maps).

203 3.1 Geological setting

204 The Shuping landslide is a chair-shaped slope that dips 20° to 30° to the north, toward the
205 Yangtze River (Fig. 7). The landslide is bounded on the east and west by two topographic gutters.
206 The altitude of its crown is 400 m above sea level (ASL), while its toe is about 70 m ASL, which is
207 now submerged by the reservoir, level of which varies annually between 145 and 175 m ASL (Fig. 8).
208 Borehole and inclinometer data (Lu et al. 2014) indicate that there are two major slide surface within
209 the west part of the slope and the upper rupture zone divides the slide mass into two parts (see Fig. 7).
210 The whole slide mass has a thickness of 30-70 m, a N-S length of about 800 m and W-E width of
211 approximately 700 m, constituting a total volume of ~ 27.5 million m^3 , of which 15.8 million m^3
212 represents the main slide mass.



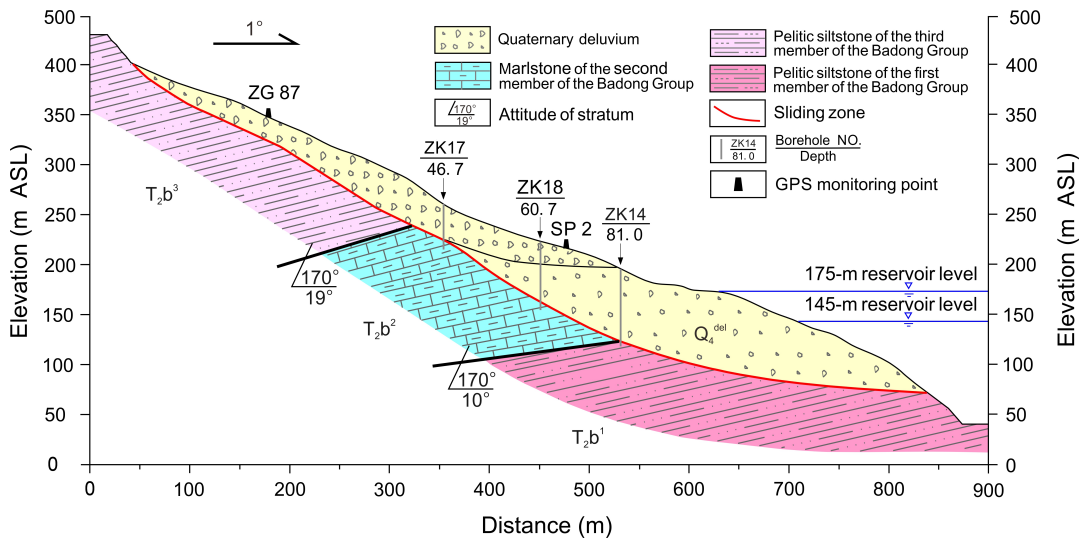
213 Shuping landslide is situated on an anti-dip bedrock of marlstone and pelitic siltstone of the
 214 Triassic Badong Group (T_2b) (Fig. 9). The upper part of the slide mass is mainly composed of yellow
 215 and brown silty clay with blocks and gravels, while the lower part of the slide mass mainly consists
 216 of dense clay and silty clay with gravels, with a thickness of about 50 m on average. The deep
 217 rupture zone is a 0.6~1.7 m layer that extends along the surface of bedrock, and consists of
 218 yellowish-brown to steel gray silty clay. The upper rupture zone in the west part has similar
 219 composition and has an average thickness of 1.0-1.2 m. The dip angle of the slide surface decreases
 220 gradually from the rear to the front (Fig. 9), so the driving-locking model is appropriate for Shuping
 221 landslide. Before reservoir impoundment, boreholes ZK17 and ZK18 were dry but borehole ZK14
 222 contained groundwater near the rupture zone.



223

224

Fig. 8 Engineering geology map of Shuping landslide



225

226

Fig.9 Geological profiles along section A-A' as shown in Fig. 8

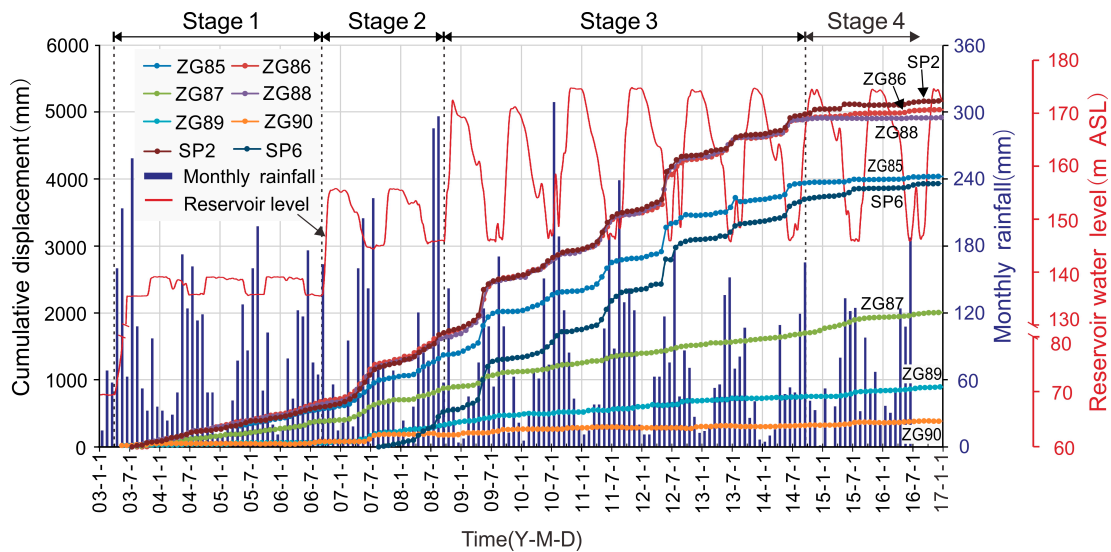
227 **3.2 Monitoring instrumentation**

228 The displacement monitoring system of Shuping landslide consists of 11 global positioning
 229 system (GPS) survey points, three of which are datum marks that were installed on stable ground
 230 outside the landslide area with the remainder being on the main slide mass (Fig. 8). Seven of the GPS
 231 monitoring points (SP2, ZG85, ZG86, ZG87, ZG88, ZG89 and ZG90) were set in June 2003 and
 232 GPS monitoring points SP6 was set in August 2007. All the GPS monitoring points were surveyed
 233 every half month, and the system was upgraded to automatic, real-time monitoring in June 2012. The
 234 daily rainfall records are obtained from the Meteorological Station near the Shuping landslide
 235 (source: <http://cdc.nmic.cn/>). Daily reservoir level is measured by China Three Gorges Corporation
 236 (source: <http://www.ctg.com.cn/inc/sqsk.php>).



237 3.3 Engineering activity

238 The evolution of Shuping landslide is related to four stages of human activity (Fig. 10). The first
239 stage was the 139 m ASL trial reservoir impoundment (from April 2003 to September 2006). The
240 reservoir water level was lifted from 69 to 135 m ASL and then changed between 135 and 139 m
241 ASL. The second stage was 156 m ASL trial reservoir impoundment (from September 2006 to
242 September 2008). The reservoir water level was raised from 139 to 156 m ASL, and then varied
243 annually between 145 and 156 m ASL. The third stage was 175 m ASL trial reservoir impoundment.
244 This stage began when the reservoir water level was raised to 175 m ASL, and thereafter managed to
245 annually varied between 145 and 175 m ASL (Tang et al., 2019). During the fourth stage, an
246 engineering project for controlling the deformation of Shuping landslide was conducted in
247 September 2014 and completed in June 2015.



248

249

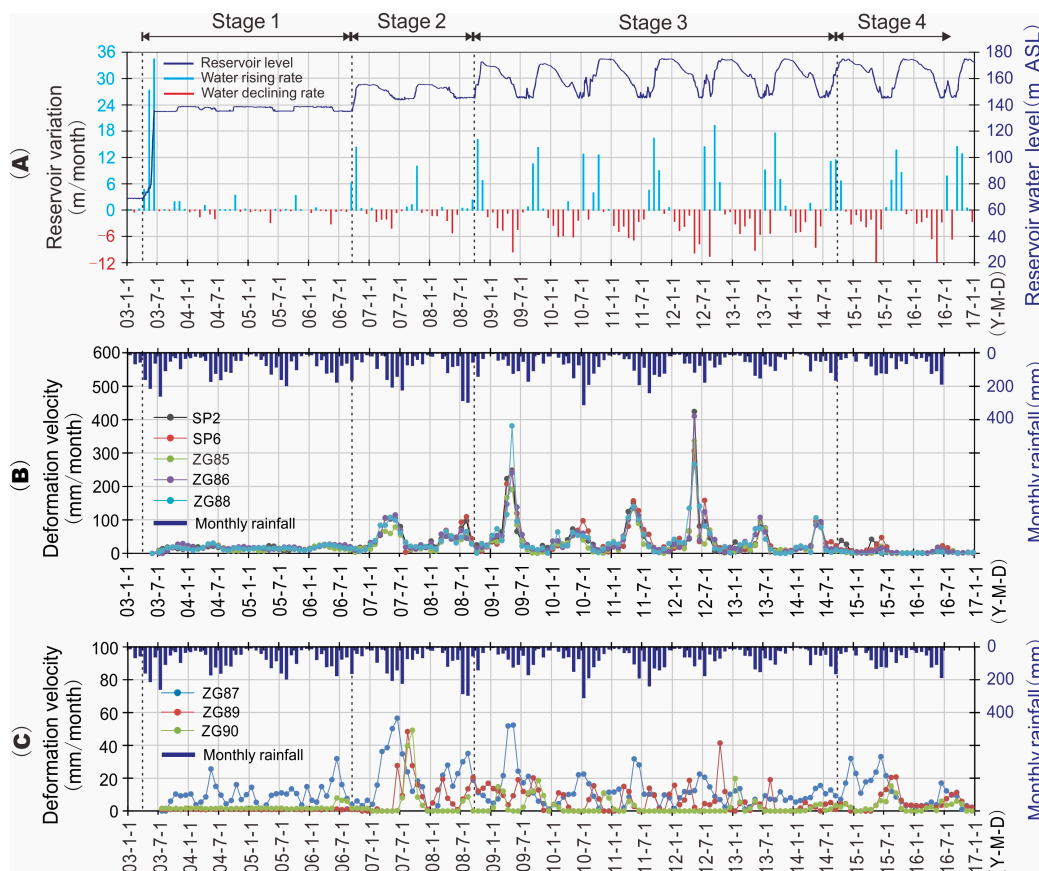
Fig. 10 Monitoring data for Shuping landslide from 2003 to 2016.



250 **4 Field observational results**

251 **4.1 Overall deformation feature**

252 According to the deformation features revealed by the GPS monitoring system (Fig. 10, Fig. 11)
253 and field investigations, the main slide mass can be divided into a main deformation area and a
254 secondary deformation area (Fig. 8). The main deformation area underlies most of the area and has a
255 cumulative displacement up to 4-5 m, as measured at sites ZG85, ZG86, ZG88, SP2 and SP6. During
256 the 13-year monitoring period point SP2 underwent the largest cumulative displacement (5.168 m),
257 followed by ZG86 and ZG88 which recorded 5.039 m and 4.919 m, respectively. Deformations were
258 essentially synchronous at the monitoring sites as indicated by the similar shape of their cumulative
259 displacement curves, which typically show steady rises in the first impoundment stage, step-like
260 trends in the second and third impoundment stages, and flat trends after the engineering treatment.
261 Deformations were smaller and steadier in the secondary deformation area, as indicated by gentle
262 cumulative displacement curves at ZG89, ZG90, and ZG87, which recorded cumulative
263 displacements of 0.5-2 m during 2003 to 2016.



264

265 **Fig. 11** Time series of reservoir level, rainfall and landslide displacement from 2003 to 2016. (A)
266 Reservoir water levels and variation rates (positive for level rise, negative for level drop); (B)
267 Deformation velocity of the GPS points in the main deformation area and monthly rainfall; (C)
268 Deformation velocity of the GPS points in secondary deformation area and monthly rainfall.

269 4.2 Deformation feature in different stages

270 After the reservoir level first rose to 135 m ASL in June 2003, the main deformation area
271 deformed at an average velocity of 15.6 mm/month until September 2006, with each site recording
272 rather steady displacement curves whose tiny or nonexistent steps correspond to the small annual



273 variations in reservoir level. In contrast, no obvious deformation occurred during Stage 1 at ZG89
274 and ZG90 in the secondary deformation area.

275 During the earliest two months of Stage 2 (September, October 2006), when the reservoir level
276 first rose to 156 m ASL, deformation velocities of the main deformation area decreased to 13.4 and
277 9.7 mm/month respectively, indicating that slide mass stability had improved. For the next two
278 months (November, December) the velocity increased to 11.5 and 14.3 mm/month, as the reservoir
279 level was steady at 156 m ASL. During the subsequent drawdown period when the reservoir level
280 dropped to 145 m ASL in 2007, the deformation velocity increased to a maximum of about 100
281 mm/month (Fig. 11), resulting in an average “jump” of 458 mm in the cumulative displacement
282 curve, which then became flat while the reservoir remained at 145 m (Fig. 10).

283 During the beginning of Stage 3 when the reservoir first rose to nearly 175m in October 2008,
284 the deformation velocity of the main deformation area decreased to 12.7 mm/month, compared to 65,
285 74, 32 mm/month in the previous three months. Shortly after the reservoir rose to its highest level,
286 the level underwent a gradual decline and the deformation velocity increased steadily. The maximum
287 deformation velocity reached 378.6 mm/month at ZG88 in May 2009 when the water level declined
288 rapidly, a rate almost four times higher than when the reservoir dropped from 156 to 145 m ASL in
289 2007. Then the deformation velocity decreased to a relatively low value when the water level was
290 steady at 145 m ASL (Fig. 11B).

291 In the subsequent 6 years of Stage 3 the reservoir level underwent a series of similar annual
292 variations, and the slide mass responded with a series of deformation “jumps”. During these cycles,

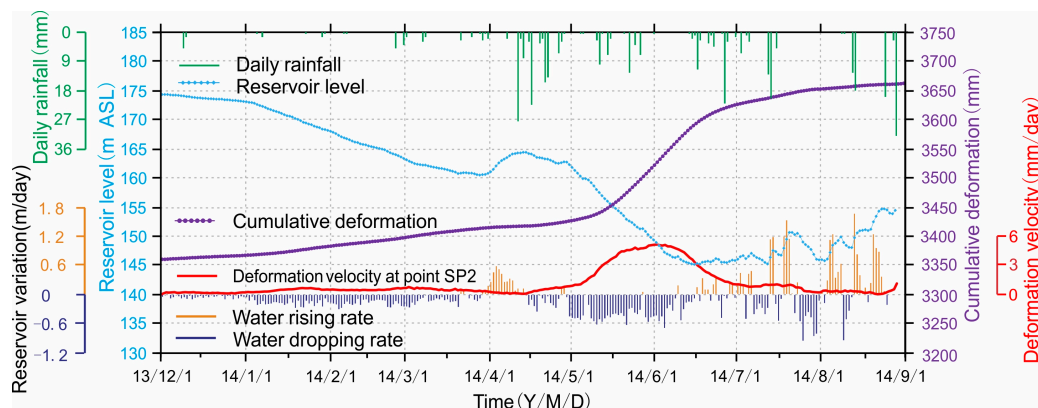


293 the deformation velocity decreased as the reservoir rose, maintained low values when the reservoir
294 remained high, began to increase as drawdown began, and attained the values up to 165 mm/month
295 when drawdown was rapid. The corresponding cumulative deformation curves featured obvious
296 “jumps” during drawdown periods, then became relatively flat as the reservoir was maintained at the
297 low level of 145 m ASL. Clearly, these results show that deformation velocity is high during
298 reservoir drawdown and low during reservoir rise.

299 After the engineering treatment was completed in June 2015, the “jumps” in the cumulative
300 displacement curves disappeared and the curves became very flat (Fig. 10). The deformation was
301 reduced to a low level of 4.1 mm/month in the main deformation area, demonstrating effective
302 treatment.

303 **4.3 Effect of water-level fluctuation and rainfall on the deformation of Shuping landslide**

304 The largest “jump” in the cumulative displacement curves averaged 479 mm and occurred in
305 May to June, 2012, while the second was the jump of 458 mm in May to June, 2009. These periods
306 corresponded with the two highest drawdown rates of 9.67 and 9.38 m/month, respectively (Fig.
307 11A). During these two years, rainfall amounts were relatively low with monthly maxima of 180
308 mm/month in 2009 and 190 mm/month in 2012 (Fig. 11). These data clearly demonstrate that the
309 deformation of Shuping landslide is primarily driven by reservoir level variations and not by rainfall.
310 This relationship is also confirmed by the low deformation velocities and flat cumulative
311 displacement curves during the July and August peak of the rainy season, when the reservoir is held
312 at its lowest level.



313
314 **Fig. 12** Monitoring data of GPS point SP2 on the middle part of slide mass, from December 2013 to
315 September 2014.

316 Figure 12 clarifies the influence of reservoir level and rainfall on landslide deformation. In
317 December 2013, the reservoir level dropped at an average rate of 0.041 m/day, and the corresponding
318 deformation velocity was 0.22 mm/day. In the subsequent three months, the drawdown rate of the
319 reservoir level increased to 0.147 m/day, and the deformation velocity rose to 0.54 mm/day. During
320 March 2014, the deformation velocity decreased as the water level increased, even though intense
321 rainfalls were recorded during this period (up to 27.5 mm/day). In the following rapid drawdown
322 period (0.419 m/day) from May to June, the deformation velocity increased to about 5 mm/day.
323 Subsequently, the deformation velocity decreased to less than 1.2 mm/day as the water level
324 remained low, although rainfall was abundant. These details confirm that the deformation velocity of
325 the Shuping landslide is positively related to the drop rate of the reservoir, with rainfall having little
326 effect.

327 Unlike the flat displacement curves and low deformation velocity in other years when the
328 reservoir level was steady at the lowest annual level in July and August, deformation velocities were
329 large in 2008 and 2010 (65.0 and 73.8 mm/month in July and August 2008; 58.4 mm/month in July



330 2010, about half of the average highest monthly deformation velocity, 165 mm/month, during rapid
331 draw down period). Very heavy rainfall was recorded during those periods, up to 300 mm/month.
332 However, August 2011 had the next heaviest rainfall of 250 mm/month, yet the cumulative
333 displacement curve remained flat and the deformation velocity was low (22.2 mm/month). These
334 data illustrate that heavy rainfall can decrease landslide stability and accelerate deformation, but
335 nevertheless is a secondary factor. The difference in the displacement velocity between the months
336 with the highest (2008, 2010) and the second highest (2011) levels of rainfall suggests that a
337 threshold exists, with rainfall exceeding this value having a significant effect but with less having
338 little significance. This threshold appears to be about 250-300 mm/month.

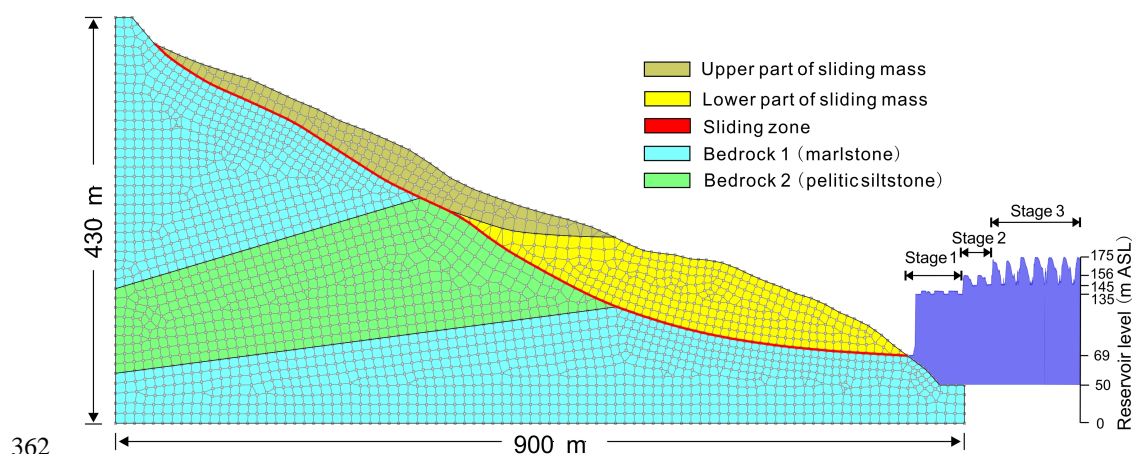
339 **5 Numerical simulation**

340 In this section, groundwater flow in the Shuping slope under the variation of the reservoir level
341 is simulated to assist the driving-locking model to explain the deformation process of Shuping
342 landslide. Seepage simulation is performed by the SEEP/W module of GEOSTUDIO software (see
343 <http://www.geoslope.com>). The deformation state of the landslide is usually regarded as the
344 performance of the landslide stability state (Wang et al., 2014; Huang et al., 2017). Thus, the Fos
345 (Safety of factor) of the Shuping landslide is calculated with the simulated groundwater level, to
346 evaluate the stability of the Shuping landslide under various impoundment scenarios. In this study,
347 the Fos of the Shuping landslide is calculated by Morgenstern-Price method (Zhu et al., 2005) using
348 the SLOPE/W module of GEOSTUDIO software. Different evaluation method for landslide stability
349 will lead to different value of Fos ; thus we only employ the calculated values of Fos to investigate



350 the variation trend of the landslide stability.

351 Figure 13 shows the numerical simulation model of the Shuping landslide, whose framework is
352 based on the geological profile map in Fig. 9. The slope was divided into six regions composed of
353 five materials with different properties (Table 1). Zero flux boundary conditions were assigned along
354 the bottom horizontal and the right vertical boundaries. A constant water head was applied at the left
355 vertical boundary assuming that it is sufficiently far from the reservoir to not be affected by
356 reservoir-level variations. A series of inverse modelling tests and water tables at the boreholes were
357 adopted to determine the constant water head at the left vertical boundary. The optimum water head
358 at the left boundary is 230 m ASL. The hydrograph of TGR from January 1, 2003 to September 10,
359 2014 (Fig. 14(A)) and generalized hydrograph of the trial impoundment at 175 m ASL (Fig. 14(B))
360 were used to define the right boundary adjacent to the reservoir. Initial conditions were defined using
361 the water tables revealed by boreholes.



362
363 **Fig. 13.** Numerical simulation model of seepage for Shuping landslide.



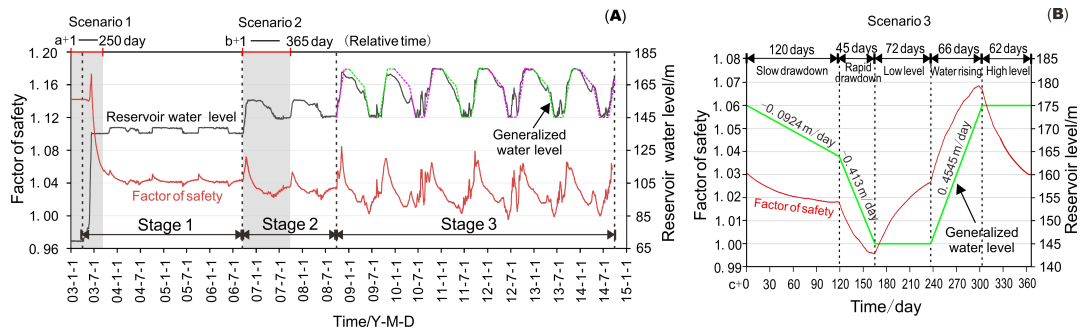
364

Table 1 Hydrologic and mechanical properties of Shuping landslide

Location	Material	Saturated conductivity k_s (m/day)	Unit weight γ (kN/m ³)	cohesion c' (kPa)	friction angle ϕ' (°)
Upper part of slide mass	Silty clay with blocks and gravels	4.95 ^a	20.3 ^a	/	/
Lower part of slide mass	Silty clay with gravels	3.90 ^a	20.3 ^a	/	/
Rupture zone	Silty clay	$2.98 \cdot 10^{-2}$ ^b	/	25.7 ^a	20.4 ^a
Bedrock 1	Marlstone	$1.47 \cdot 10^{-4}$ ^b	/	/	/
Bedrock 2	Pelitic siltstone	$8.99 \cdot 10^{-5}$ ^b	/	/	/

365 ^a Provided by Hubei Province Geological Environment Terminus (2003)

366 ^b Values of similar material from literature (Hu et al., 2015)



367

368 **Fig. 14** (A) Time series of reservoir level and corresponding calculated *Fos* of Shuping landslide

369 from January 1, 2003 to September 10, 2014. (B) Generalized annual variation curve of the reservoir

370 level obtained by fitting the real water level from 2008 to 2014 (Stage 3) and the corresponding time

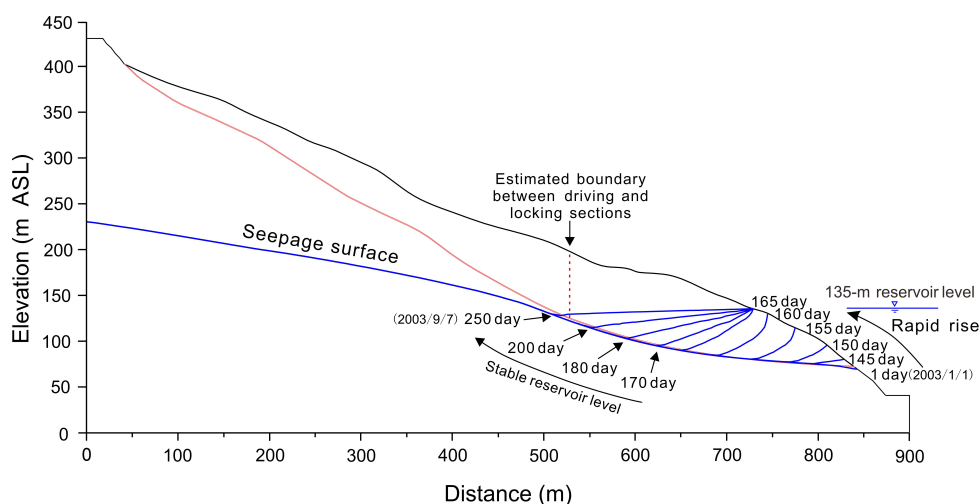
371 series of the calculated *Fos* of Shuping landslide.

372 5.1 Scenario 1: first trial impoundment at 139 m ASL

373 From April 10 to June 11, 2003 (a+100~162 day), the reservoir level rose rapidly from 69 to 135



374 m ASL. Fig. 15 shows that, during this period, groundwater storage increased in the toe of the slide
375 mass and within the lower part of the locking section, increasing buoyancy forces that destabilized
376 the slope. In contrast, the inwardly-directed flow created a seepage force directed towards the slope,
377 increasing stability. Owing to the high hydraulic gradient, the stabilizing effect of the seepage force
378 on the slope prevails over the destabilization due to increased buoyancy, so slope stability was
379 improved during this phase, as indicated by the increase in Fos up to 1.17 (Fig. 14).



380
381 **Fig. 15** Simulated groundwater tables during the period of rapid reservoir rise from January 1, 2003
382 to September 7, 2003.

383 In the following period (a+163 day~), the reservoir level was maintained around 135 m ASL.
384 The water table progressively rose until it approximated the reservoir level. During this period, the
385 slope of the water table front decreased gradually, leading to a decrease of the seepage force in the
386 slope. At the same time, the buoyancy uplift effect increased steadily in the locking section as the
387 groundwater table rose (Fig. 15). The combination of a decreased seepage force and the increased
388 buoyancy led to a decrease in slope stability during this phase, so the Fos dropped below its initial

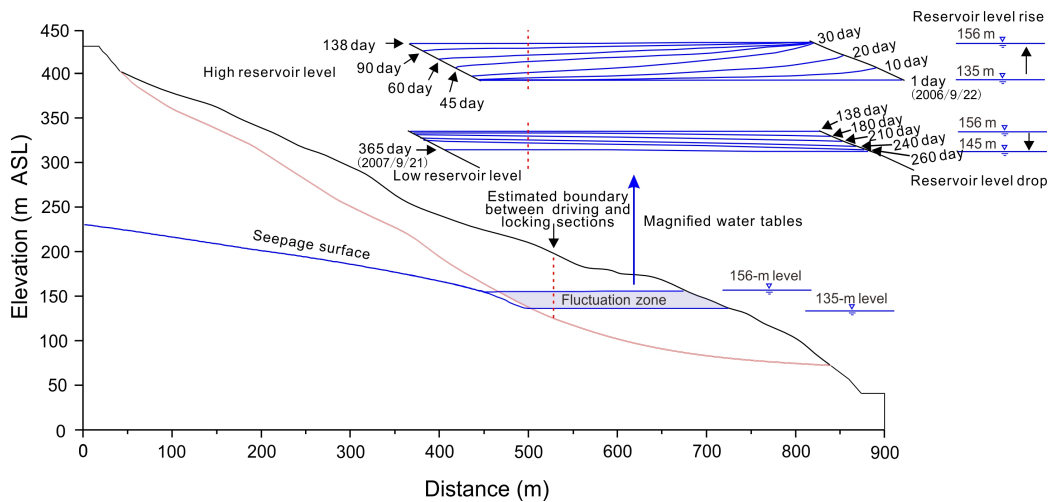


389 value of 1.142. Afterwards, the slope stability continued to decrease until the new but temporary state
390 of equilibrium was reached. The safety factor was around 1.045 as the reservoir level was maintained
391 around 135 m ASL.

392 The delay between the reservoir impoundment and the decrease in stability is consistent with the
393 creation of obvious cracks after the reservoir rose to 135 m ASL (Wang et al., 2007). The famous
394 Qianjiangping landslide (Fig. 2), which is located near the Shuping landslide and has similar
395 geological setting, occurred one month (13 July 2003) after the reservoir first rose to 135 m ASL
396 (Xiao et al., 2007).

397 **5.2 Scenario 2: first trial impoundment at 156 m ASL**

398 During the periods when the water level rose from 135 m ASL to 156 m ASL (b+1~30 day) (Fig.
399 16), and stayed stable at 156 m ASL (b+30~138 day), the effects of ground water level change on the
400 stability of Shuping landslide were similar to the effects in scenario 1. When the reservoir level
401 dropped from 156 to 145 m ASL during the drawdown period of February to June (b+138~260 day),
402 groundwater flow towards the reservoir, thus creating an outward, destabilizing seepage force on the
403 slope. The computed factor of safety decreased gradually from 1.070 to 1.025, in agreement with the
404 observed increase in deformation velocity during this period. As the reservoir level was then
405 maintained at 145 m ASL (b+260~365 day), the transient seepage gradually transitioned to
406 steady-state seepage, accompanied by a progressively decline of the water table in the inside part of
407 the fluctuation zone, a weakening of the destabilizing effect of the seepage force, and a result of
408 increase in slope stability ($F_{os}=1.035$).



409

410 **Fig. 16** Simulated groundwater tables as the variation of reservoir water level from 22 September
411 2006 to 21 September 2007.

412 **5.3 Scenario 3: trial impoundment at 175 m ASL**

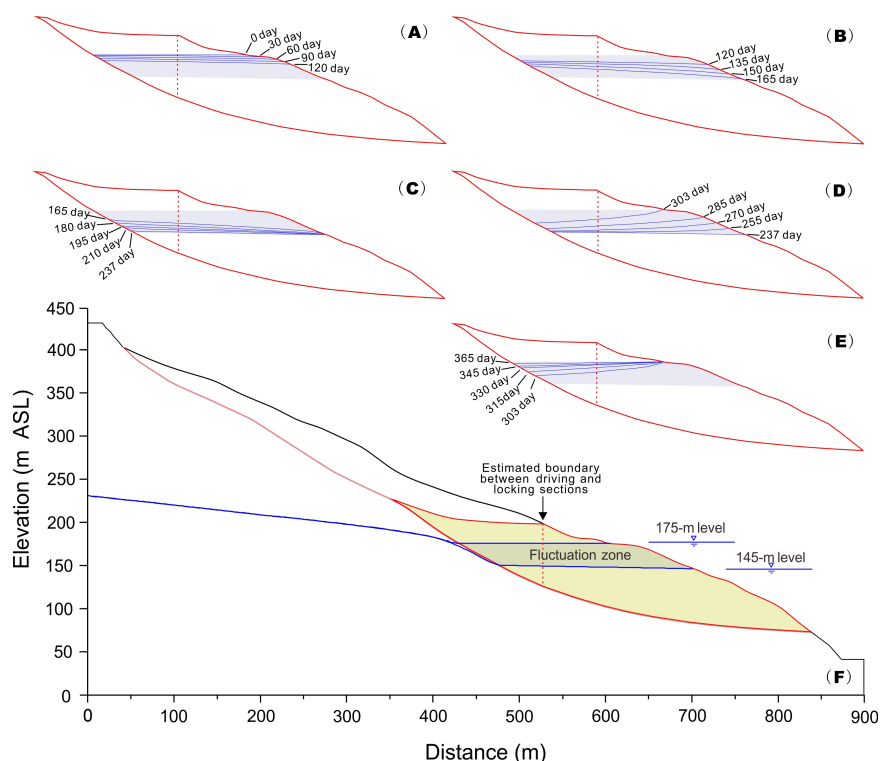
413 During 2008 to 2014 the reservoir level periodically fluctuated between 145 and 175 m ASL
414 (Stage 3), in accordance with a generalized annual water level variation curve that consists of five
415 phases (Fig. 13(B)).

416 During the slow drawdown period, the groundwater storage in the driving section is reduced by
417 an amount that approximately matches the reduction in the locking section (Fig. 17(A)), so the effect
418 of buoyancy forces on slope stability is small. Moreover, because drawdown is slow, groundwater
419 gradients are also low, limiting the magnitude of destabilizing seepage forces. Thus, the safety factor
420 of the slope decreases from 1.031 to 1.018 with only a modest amount (Fig. 14(B)).

421 During the rapid drawdown phase, groundwater gradients are steeper and produce large,
422 destabilizing seepage forces on the slope. The sharp decline of slope stability (Fig. 17(B)) is
423 consistent with the observed high deformation velocity during this phase. The slope stability



424 becomes least ($Fos=0.995$) as the reservoir declines to its lowest level of 145 m ASL, when a
 425 maximum difference of 14 m is computed for groundwater levels in the slide mass (Fig. 17(B)).
 426 Although the decreased buoyancy of the locking section makes an offsetting contribution to slope
 427 stability, its magnitude is small compared to that of destabilizing seepage forces.



428
 429 **Fig. 17** Simulated groundwater tables over the period of generalized annual variation of reservoir
 430 water level in Stage 3. Gray shaded zone depicts the 145 to 175 m elevation interval. (A) slow
 431 drawdown phase; (B) rapid drawdown phase; (C) low level phase; (D) water level rising phase; (E)
 432 high water level phase

433 In the following three phases, representing the low water, rising and high water phases, the
 434 characteristics of the slope vary in a manner similar to those modeled in scenario 2. The stability of



435 the landslide (see Fig. 14(B)) recovers gradually from 0.995 to 1.027 in the low water level phase,
436 due to the dissipation of destabilizing seepage forces (Fig. 17(C)). Slope stability then increases
437 rapidly as the reservoir level rises rapidly, when the seepage force reverses to become directed into
438 the slope (Fig. 17(D)). The slope obtains the highest stability with Fos value of 1.067 when the water
439 level rises to the highest level 175 m ASL. Slope stability then decreases gradually as that seepage
440 force declines (Fig. 17(E)). All these results agree with the observed variations in deformation
441 velocity of the Shuping landslide (Sec. 4.2).

442 In summary, during periods of reservoir drawdown and rise, the seepage force plays a dominant
443 role in the stability of Shuping landslide, but being negative in drawdown period and positive in the
444 rising period. In contrast, buoyancy effects become increasingly important during periods of steady
445 reservoir levels, as seepage forces steadily decrease.

446 **6 Discussion**

447 This deformation of the Shuping landslide is a function of reservoir levels but probably also
448 depends on the hydraulic character of its constituent material. The lower part of the slide mass that is
449 subject to reservoir level fluctuation is mainly composed of dense silty soil with very low hydraulic
450 conductivity. During periods of rapid change in reservoir level, large differences in groundwater head
451 can be formed in such material, generating large seepage pressures that can either destabilize or
452 stabilize the mass, depending on whether the reservoir is rising or falling. On the other hand, low
453 permeability materials impede rainfall infiltration, rendering the landslide little influenced by rainfall.
454 Consequently, variations of the reservoir level and their attendant seepage forces dominate the
455 deformation of Shuping landslide.

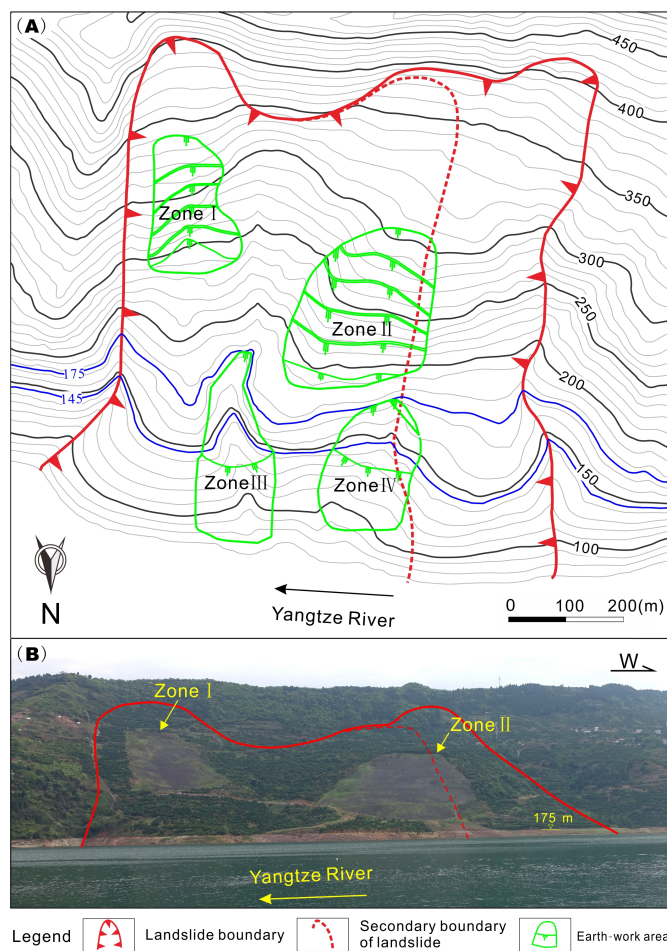


456 The evolutionary trend of the Shuping landslide under periodical water-level variations is a
457 significant issue. Shuping landslide has already moved horizontally by as much as ~5 m. As the mass
458 has descended, more material has migrated from the driving section to the locking section. The
459 reduction in weight of the driving section and the increased weight of the locking section has likely
460 improved slope stability. Support for this inference is found in the decreased deformation velocities
461 and decreased magnitude of the “jumps” in the observed, step-like cumulative curves in 2013 and
462 2014 (Fig. 10).

463 Based on this observation and on the results of the driving-locking model, two approaches are
464 recommended to control the deformation of huge reservoir landslides where the reinforcement
465 structures are difficult to construct. One method to improve stability is to transfer earth mass from
466 the driving section to the locking section of the slide mass. The other is to use drains or pumps to
467 lower the water levels inside the slope, in order to reduce differences in groundwater head during
468 periods of reservoir drawdown. The first approach has in fact been adopted to enhance the stability of
469 Shuping landslide. Fig. 18(A) presents the layout of the engineering treatment and Fig. 18(B) is the
470 subsequent photo of Shuping landslide. Zones I and II are the areas of load reduction, located in
471 the driving section of the slide mass. The earth mass of Zone I ($\sim 1.8 \times 10^5 \text{ m}^3$) and Zone II
472 ($\sim 4.0 \times 10^5 \text{ m}^3$) were transferred to Zones III and IV respectively, which are located in the locking
473 section that is mostly below reservoir level in the photo (Fig. 18(B)). The transfer operation began in
474 September 2014 and was completed in June 2015. Monitoring data show that the deformation
475 velocity was significantly reduced to low values (about 4.1 mm/month in the main deformation area),
476 demonstrating the effectiveness of the engineering treatment. These approaches are more economical
477 and require a shorter construction period than many commonly-used remediation methods such as
478 the construction of stabilizing piles. Most importantly, these treatments are feasible for many other



479 large reservoir landslides.



480

481 **Fig. 18** Topography of Shuping landslide before (A) and after (B) engineering treatment, which

482 involved the transfer of earth from Zones I and II to Zones III and IV.

483 7 Conclusions

484 A driving-locking model is presented to elucidate the deformation mechanism of reservoir
485 landslides, as exemplified by Shuping landslide. The deformation velocity of Shuping landslide is
486 closely related to the variations in the level of the Three Gorges reservoir. Rainfall effects are limited



487 in comparison, perhaps due to the low hydraulic conductivity of the slide material. Rapid reservoir
488 drawdown produces large, destabilizing seepage forces in the slope of the slide mass, as evidenced
489 by large increases of its deformation velocity. In contrast, rising reservoir levels reverse the direction
490 of the seepage force, improving slope stability and decreasing the deformation velocity. The
491 buoyancy effect on the locking section decreased the slope stability when the reservoir first rose to
492 135 m ASL, but this effect has diminished as the reservoir has attained higher levels that buoy both
493 the driving and locking sections.

494 Monitoring data, the driving-locking model, and a successful engineering treatment suggest two
495 means to increase the stability of landslides in the TGR area. Recommended approaches are: 1)
496 transferring earth mass from the driving section to the locking section; and 2) lowering the ground
497 water levels inside the slope by drains or by pumping during periods of reservoir drawdown. The
498 first approach was successfully applied to the Shuping landslide and could be used to treat many
499 other huge landslides in the Three Gorges Reservoir area.

500 **Data availability**

501 The study relied on the observation data from Department of Land and Resources of Hubei
502 Province, China.

503 **Competing interests**

504 The authors declare that they have no conflict of interest.



505 **Acknowledgements**

506 This work was supported by the National Key R&D Program of China (No. 2017YFC1501305);
507 the Fundamental Research Funds for the Central Universities, China University of Geosciences
508 (Wuhan) (No. CUGCJ1701); and the National Natural Science Foundation of China (Nos. 41630643,
509 41827808, 41502290).

510



511 **9 References**

- 512 1. Casagli, N., Rinaldi, M., Gargini, A., and Curini, A.: Monitoring of pore water pressure and
513 stability of streambanks: results from an experimental site on the Sieve River, Italy, *Earth Surface*
514 *Processes and Landforms*, 24, 1095-1114, [https://doi.org/10.1002/\(SICI\)1096-9837\(199911\)24:](https://doi.org/10.1002/(SICI)1096-9837(199911)24:12<1095::AID-ESP37>3.0.CO;2-F)
515 [12<1095::AID-ESP37>3.0.CO;2-F](https://doi.org/10.1002/(SICI)1096-9837(199911)24:12<1095::AID-ESP37>3.0.CO;2-F), 1999.
- 516 2. Chang, S.B., Zhang, S.M. and Xiang B.: *Engineering geology manual*. China Architecture &
517 Building Press, Beijing, 2007 (in Chinese).
- 518 3. Cojean, R., and Cai, Y.J.: Analysis and modeling of slope stability in the Three-Gorges Dam
519 reservoir (China) -The case of Huangtupo landslide, *Journal of Mountain Science*, 8, 166-175,
520 <https://doi.org/10.1007/s11629-011-2100-0>, 2011.
- 521 4. Du, J., Yin, K., and Lacasse, S.: Displacement prediction in colluvial landslides, three Gorges
522 reservoir, China, *Landslides*, 10, 203-218, <https://doi.org/10.1007/s10346-012-0326-8>, 2013.
- 523 5. Dumperth, C., Rohn, J., Fleer, A., and Xiang, W.: Local-scale assessment of the displacement
524 pattern of a densely populated landslide, utilizing finite element software and terrestrial radar
525 interferometry: a case study on Huangtupo landslide (PR China), *Environmental Earth Sciences*,
526 75, 880, <http://doi.10.1007/s12665-016-5475-y>, 2016.
- 527 6. Froude, M. J., and Petley, D. N.: Global fatal landslide occurrence from 2004 to 2016, *Natural*
528 *Hazards and Earth System Sciences*, 18, 2161-2181, <https://doi.org/10.5194/nhess-18-2161-2018>,
529 2018.
- 530 7. Hu, X. W., Tang, H. M., and Liu, Y. R.: Physical model studies on stability of Zhaoshuling
531 landslide in area of Three Gorges Reservoir, *Chinese Journal of Rock Mechanics and Engineering*,



- 532 24, 2089-2095, 2005 (in Chinese).
- 533 8. Huang, B. L., Yin, Y. P., Wang, S. C., Tan, J., M., and Liu, G. N.: Analysis of the Tangjiaxi
534 landslide-generated waves in the Zhexi Reservoir, China, by a granular flow coupling model,
535 Natural Hazards and Earth System Sciences, 17, 657-670,
536 <https://doi.org/10.5194/nhess-17-657-2017>, 2017.
- 537 9. Huang, D., and Gu, D. M.: Influence of filling-drawdown cycles of the Three Gorges reservoir
538 on deformation and failure behaviors of anacinal rock slopes in the Wu Gorge, Geomorphology,
539 295, 489-506, <https://doi.org/10.1016/j.geomorph.2017.07.028>, 2017.
- 540 10. Huang, F. M., Huang, J. S., Jiang, S. H., and Zhou, C. B.: Landslide displacement prediction based
541 on multivariate chaotic model and extreme learning machine, Engineering Geology, 218, 173-186,
542 <https://doi.org/10.1016/j.enggeo.2017.01.016>, 2017.
- 543 11. Hubei Province Geological Environment Terminus: Survey report of Shuping landslide in Three
544 Gorges Reservoir area, Zigui, Hubei Province, China, 2013 (in Chinese).
- 545 12. Jia, G. W., Zhan, T. L., Chen, Y. M., and Fredlund, D. G.: Performance of a large-scale slope
546 model subjected to rising and lowering water levels, Engineering Geology, 106, 92-103,
547 <https://doi.org/10.1016/j.enggeo.2009.03.003>, 2009.
- 548 13. Junfeng Z., Xiangyue M., and Erqian Z.: Testing study on landslide of layered slope induced by
549 fluctuation of water level, Chinese Journal of Rock Mechanics and Engineering, 23, 2676-2680,
550 2004 (in Chinese).
- 551 14. Lambe, T. W., and Whitman, R. V.: Soil mechanics SI version, John Wiley & Sons, 2008.
- 552 15. Lane, P. A., and Griffiths, D. V.: Assessment of stability of slopes under drawdown conditions,



- 553 Journal of geotechnical and geoenvironmental engineering, 126, 443-450,
554 [https://doi.org/10.1061/\(ASCE\)1090-0241\(2000\)126:5\(443\)](https://doi.org/10.1061/(ASCE)1090-0241(2000)126:5(443)), 2000.
- 555 16. Li, D., Yin, K., and Leo, C.: Analysis of Baishuihe landslide influenced by the effects of reservoir
556 water and rainfall, Environmental Earth Sciences, 60, 677-687,
557 <https://doi.org/10.1007/s12665-009-0206-2>, 2010.
- 558 17. Liao, H. J., Sheng, Q., Gao, S. H., and Xu, Z. P.: Influence of drawdown of reservoir water level
559 on landslide stability, Chinese Journal of Rock Mechanics and Engineering, 24, 3454-3458, 2005
560 (in Chinese).
- 561 18. Lu, S. Q., Yi, Q. L., Yi, W., Huang, H. F., and Zhang, G. D.: Analysis of deformation and failure
562 mechanism of Shuping landslide in Three Gorges reservoir area. Rock and Soil Mechanics 35(4),
563 1123-1130, 2014 (in Chinese).
- 564 19. Lu, T.: Study of Formation Mechanism and Later Trend Prediction of Fanjiaping Landslide and
565 Baishuihe Landslide, Dissertation, China Three Gorges University (in Chinese).
- 566 20. Ma, J. W., Tang, H. M., Hu, X. L., Bobet A., Zhang, M., Zhu, T. W., Song, Y. J., and Eldin M. A.
567 E.: Identification of causal factors for the Majiagou landslide using modern data mining methods,
568 Landslides, 14, 311-322, <https://doi.org/10.1007/s10346-016-0693-7>, 2017.
- 569 21. Miao, F. S., Wu, Y. P., Li, L. W., Tang, H. M., and Li, Y. N.: Centrifuge model test on the
570 retrogressive landslide subjected to reservoir water level fluctuation, Engineering geology, 245:
571 169-179, <https://doi.org/10.1016/j.enggeo.2018.08.016>, 2018.
- 572 22. Paronuzzi, P., and Bolla, A.: The prehistoric Vajont rockslide: an updated geological model,
573 Geomorphology, 169, 165-191, <https://doi.org/10.1016/j.geomorph.2012.04.021>, 2012.



- 574 23. Qin, H. B.: The Mechanism of Landslide Influenced by Rainfall and Reservoir Water Level
575 Fluctuation and Renewed Criterion Research in Three-Gorges Reservoir, Dissertation, China
576 Three Gorges University, 2011(in Chinese).
- 577 24. Ren, F., Wu, X. L., and Zhang, K. X., and Niu, R. Q.: Application of wavelet analysis and a
578 particle swarm-optimized support vector machine to predict the displacement of the Shuping
579 landslide in the Three Gorges, China, *Environmental earth sciences*, 73, 4791-4804,
580 <https://doi.org/10.1007/s12665-014-3764-x>, 2015.
- 581 25. Rinaldi, M., and Casagli, N.: Stability of streambanks formed in partially saturated soils and
582 effects of negative pore water pressures: the Sieve River (Italy), *Geomorphology*, 26, 253-277,
583 <https://doi.org/10.1007/s12665-014-3764-x>, 1999.
- 584 26. Rinaldi, M., Casagli, N., Dapporto, S., and Gargini, A.: Monitoring and modelling of pore water
585 pressure changes and riverbank stability during flow events, *Earth Surface Processes and
586 Landforms*, 29, 237-254, <https://doi.org/10.1002/esp.1042>, 2004.
- 587 27. Song, W. P.: The unsaturated seepage and stability analysis on slopes at river banks with the case
588 of Xicheng landslides in Yunyang. Dissertation, Chengdu University of Technology, 2011(in
589 Chinese).
- 590 28. Song, K., Wang, F. W., Yi, Q. L., and Lu, S. Q.: Landslide deformation behavior influenced by
591 water level fluctuations of the Three Gorges Reservoir (China), *Engineering Geology*, 247, 58-68,
592 <https://doi.org/10.1016/j.enggeo.2018.10.020>, 2018.
- 593 29. Song, K., Yan, E. C., Zhang, G. D., Lu, S. Q., and Y, Q. L.: Effect of hydraulic properties of soil
594 and fluctuation velocity of reservoir water on landslide stability, *Environmental earth sciences*, 74,



- 595 5319-5329, <https://doi.org/10.1007/s12665-015-4541-1>, 2015.
- 596 30. Tang, H. M., Li, C. D., Hu, X. L., Su, A. J., Wang, L. Q., Wu, Y. P., Criss, R. E., Xiong, C. R.,
597 and Li, Y. A.: Evolution characteristics of the Huangtupo landslide based on in situ tunneling and
598 monitoring, *Landslides*, 12, 511-521, <https://doi.org/10.1007/s10346-014-0500-2>, 2015.
- 599 31. Tang, H. M., Wasowski, J., and Juang, C. H.: Geohazards in the three Gorges Reservoir Area,
600 China - Lessons learned from decades of research, *Engineering Geology*, 261,
601 <https://doi.org/10.1016/j.enggeo.2019.105267>, 2019.
- 602 32. Wang, F.: Deformation prediction of Jiuxianping landslide in Yunyang Country based on
603 numerical simulation, Dissertation, Chengdu University of Technology, 2013 (in Chinese).
- 604 33. Wang, F., Zhang, Y., Wang, G., Peng, X., Huo, Z., Jin, W., and Zhu, C.: Deformation features of
605 Shuping landslide caused by water level changes in Three Gorges Reservoir area, China, *Chinese*
606 *Journal of Rock Mechanics and Engineering*, 26, 509-517, (in Chinese).
- 607 34. Wang, J. E., Xiang, W., and Lu, N.: Landsliding triggered by reservoir operation: a general
608 conceptual model with a case study at Three Gorges Reservoir, *Acta Geotechnica*, 9, 771-788,
609 <https://doi.org/10.1007/s11440-014-0315-2>, 2014.
- 610 35. Wang, H. L., and Xu, W. Y.: Stability of Liangshuijing landslide under variation water levels of
611 Three Gorges Reservoir, *European Journal of Environmental and Civil Engineering*, 17(sup1):
612 s158-s177, <https://doi.org/10.1080/19648189.2013.834592>, 2013.
- 613 36. Wen, T., Tang, H. M., Wang, Y. K., Lin, C. Y., and Xiong, C. R.: Landslide displacement
614 prediction using the GA-LSSVM model and time series analysis: a case study of Three Gorges
615 Reservoir, China, *Natural Hazards and Earth System Sciences*, 17, 2181-2198,



- 616 <https://doi.org/10.1002/esp.1042>, 2017.
- 617 37. Wu, Q., Tang, H. M., Ma, X. H., Wu, Y. P., Hu, X. L., Wang, L. Q., Criss, R. E., Yuan, Y., and Xu,
618 Y. J.: Identification of movement characteristics and causal factors of the Shuping landslide based
619 on monitored displacements, *Bulletin of Engineering Geology and the Environment*, 78,
620 2093-2106, <https://doi.org/10.1007/s10064-018-1237-2>, 2019.
- 621 38. Xiao, S. R., Liu, D. F., and Hu, Z. Y.: Study on geomechanical model of Qianjiangping landslide,
622 Three Gorges Reservoir, *Rock and Soil Mechanics*, 28, 1459-1464, 2007 (in Chinese).
- 623 39. Yin, Y., Huang, B., Wang, W., Wei, Y., Ma, X., Ma, F., and Zhao, C.: Reservoir-induced landslides
624 and risk control in Three Gorges Project on Yangtze River, China, *Journal of Rock Mechanics and*
625 *Geotechnical Engineering*, 8, 577-595, <https://doi.org/10.1016/j.jrmge.2016.08.001>, 2016.